Physics and simulation of transport processes in hybrid organic semiconductor devices

by

Ian Michael Rousseau

Submitted to the Department of Physics
in partial fulfillment of the requirements for the degree of

Bachelor of Science in Physics

at the

MASSACHUSETTS INSTITUTE OF TECHNOLOGY

June 2010

Author .....
Department of Physics
June 4, 2010

Certified by .....
Professor Vladimir Bulović
Department of Electrical Engineering and Computer Science
Thesis Supervisor

Certified by .....
Professor Marin Soljačić
Department of Physics
Thesis Supervisor

Accepted by .....
Professor David Pritchard
Senior Thesis Coordinator, Department of Physics

Physics and simulation of transport processes in hybrid organic semiconductor devices

by

Ian Michael Rousseau

Submitted to the Department of Physics
on June 4, 2010, in partial fulfillment of the
requirements for the degree of
Bachelor of Science in Physics

Abstract

Organic semiconductors and nanomaterials promise to potentially form the basis for future efficient and cost-effective large area optoelectronic devices, such as light-emitting diodes and solar cells. Although these materials' amorphous nature allow utilization of cheap, high-throughput manufacturing techniques, it poses a unique challenge: the physics of carrier and excitation transport in amorphous semiconductors is fundamentally different from their crystalline semiconductor counterparts. Excitations remain localized on single molecules or nanocrystals; the drift-diffusion equations, which describe carrier transport in delocalized states near thermal equilibrium, are no longer valid.

A computational model for device operation would give researchers a powerful tool to design and improve devices. This work presents a novel one-dimensional discrete model that combines the computational speed of simulations based on the drift-diffusion equations with the accuracy and flexibility of Monte Carlo simulations. The one-dimensional model is shown to be exactly equivalent to the drift-diffusion model in the limits of small applied field, narrow densities of state, and low carrier concentrations. In this limit, the Einstein relation for Brownian motion holds and the transport parameters in the one-dimensional discrete model can be directly estimated from experimentally-measurable quantities. The model is implemented in an object-oriented Python computational framework. Finally, two test cases are numerically studied: an initial, test device with fictitious parameters and a well-known organic light-emitting diode. Preliminary results demonstrate reproduce experimental current-voltage characteristics over a wide range of bias voltages.

Thesis Supervisor: Professor Vladimir Bulović
Title: Department of Electrical Engineering and Computer Science

Thesis Supervisor: Professor Marin Soljačić
Title: Department of Physics

Acknowledgments

I am indebted to the past and current members of the Laboratory of Organic Optoelectronics, especially Prof. Vladimir Bulovic and Drs. Alexi Arango, Vanessa Wood, Polina Anikeeva, and Conor Madigan for their generosity, kindness, and patience in teaching me about organic optoelectronics over the course of three years. I would also like to thank Prof. Marin Soljacic and Dr. Peter Bermel for being my co-advisors in the Department of Physics. I would like to acknowledge Prof. Jeffrey Grossman for helping me post the code on the National Science Foundation's NanoHub.

I thank my parents, Dean and Claire, and my sister, Marielle, for their support over the last four years. You helped me keep everything in perspective and were always willing to listen, through the good and the tough spots.

Contents

List of Figures

List of Tables

Chapter 1

Introduction

Microelectronics revolutionized life in the 20^{th} century and comprises an integral part of our lives today. Most currently available electronic devices are based upon crystalline semiconductors, such as silicon. Manufacturing microelectronics requires many high-precision steps and inputs; mining, purifying, growing crystals, slicing, photolithography, and intentional impurity doping are time- and energy-consuming processes [50]. Such expensive processing techniques have restricted applications of electronics based upon crystalline semiconductors. For example, it is not cost-effective to make large-area optoelectronic devices, such as lighting, displays, and solar cells out of these materials [14].

The demand for large-area optoelectronic devices, due to recent interest in energy efficiency and renewable energy, has forced researchers to consider new materials. In the 70s, semiconducting polymers with benzene rings were discovered [31]. Since then, researchers have fabricated electronic devices from amorphous, or disordered, films of these materials. In 1987, Tang created the first organic optoelectronic device, a light-emitting diode (LED) [51]. Organic semiconductors are appealing materials for optoelectronics because chemists can finely tune their properties and films of these materials can be deposited using low-cost manufacturing techniques, such as spin-casting, inkjet printing, and stamping [14]. Now, twenty-five years after Tang's discovery, the first organic LED (OLED) displays and lighting are nearing commercialization [48, 45, 38].

Nanotechnology, the ability to manipulate individual atoms and molecules, could provide a path to improved performance, especially in organic optoelectronics. Quantum dots, semiconductor crystals smaller than the Bohr wavelength of an electron, offer unprecedented control over optoelectronic properties; the colors, or wavelengths, at which the dots absorb and emit light are narrow-banded and can be finely tuned by changing the dots' size [19]. Hybrid electronic devices, containing both amorphous semiconductors and these nanostructured materials, show great promise for optoelectronics [3, 2, 30, 44, 53].

1.1 Motivation

The Laboratory of Organic Optoelectronics (ONELab), a division of the Research Laboratory of Electronics at MIT, fabricates solar cells, LEDs, chemical sensors, and photodetectors from films of organic semiconductors, metal oxides, and colloidal quantum dots [2, 53, 3]. The group has many promising experimental results. For example, Alexi Arango's hybrid organic semiconductor-quantum dot solar cells [3] have an open-circuit voltage, one of the three metrics of solar cell efficiency, higher than that predicted by the prevailing theory in literature [55]. A computational simulation tool could complement the group's experimental results and suggest methods to improve device efficiency.

1.2 Materials

Hybrid optoelectronic devices are composed of a stack of alternating layers of homogeneous amorphous semiconductor or nanostructured materials (Figure 1-1). Each layer ranges from tens to hundreds of nanometers in thickness, while the length and width of the whole device are on the order of centimeters. Two metal electrodes, one or both of which are optically transparent, terminate the stack, one on each end. The experimenter probes the device by attaching current-voltage probes to the electrodes and shining light on the stack.

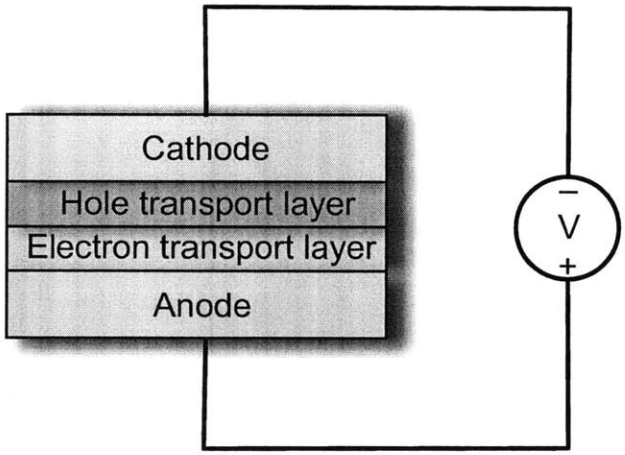

Figure 1-1: A device is a sequence of N homogeneous layers of either colloidal quantum dot film or amorphous semiconductor with two electrodes.

Different physics govern performance in each layer of the device, depending the properties of the constituent materials. Additional physical processes occur at the interfaces between layers. The following sections describe the physics of the different materials used in ONELab's devices.

1.2.1 Organic semiconductors

Although Bloch waves describe carrier behavior in crystalline inorganic semiconductors [16], this elegant theory from quantum mechanics cannot be applied to amorphous semiconductors. Thin films of organic molecules interact by van der Waals interactions because there is little wavefunction overlap between molecules [2]. Moreover, there is no long-range order, so one cannot take advantage of lattice symmetry to simplify calculation [41].

Since excitations are localized on individual molecules in organic electronics, they are described by a different language than their inorganic counterparts. The familiar holes and electrons in crystalline semiconductor physics are called positive and negative polarons in organic electronics. The addition of an electron to a molecule in the ground state forms a negative polaron, while the removal of an electron results in a

positive polaron [24]. In the context of molecular orbital theory, a positive polaron (Fig. 1-3) can be thought of as a vacancy, or hole, in the highest occupied molec-

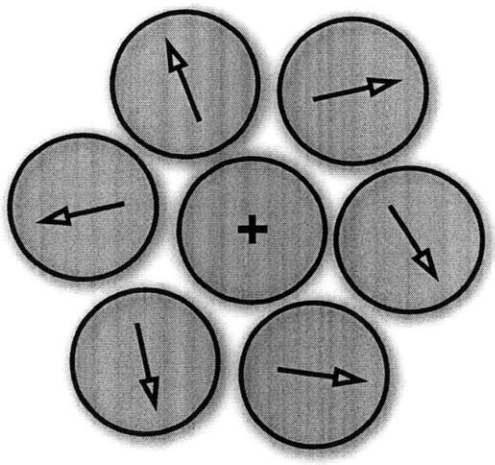

Figure 1-2: A polaron is a charged molecule and the surrounding lattice distortion created by the presence of the charge, pictured by the dipoles.

ular level (HOMO) of one molecule coupled with a local lattice distortion caused by electrostatic interactions. Likewise, a negative polaron corresponds to the addition of an electron to the lowest unoccupied molecular level (LUMO) along with its accompanying lattice distortion.

In organic optoelectronics, additional excitations called excitons are responsible for optical processes. Excitons are electrically neutral excited states formed by a bound electron-hole pair and are classified by their total spin (Fig. 1-3). An exciton with total spin quantum number $S = 1$ is called a singlet exciton, while an $S = 0$ exciton is known as a triplet exciton. Electrical dipole transitions are forbidden for triplet excitons because of quantum mechanical selection rules [16]. Thus, the radiative, electrical dipole transition rate for singlets (fluorescence) is much faster than the same transition for triplet excitons (phosphorescence)[1] [24].

Monte Carlo simulations [9, 24, 28, 37] show that transport does not occur at thermal equilibrium in organic semiconductors. Although the density of available

[1]In organic molecules with heavy metal atoms, $\vec{L} \cdot \vec{S}$ coupling can significantly increase triplets' dipole transition rates [8].

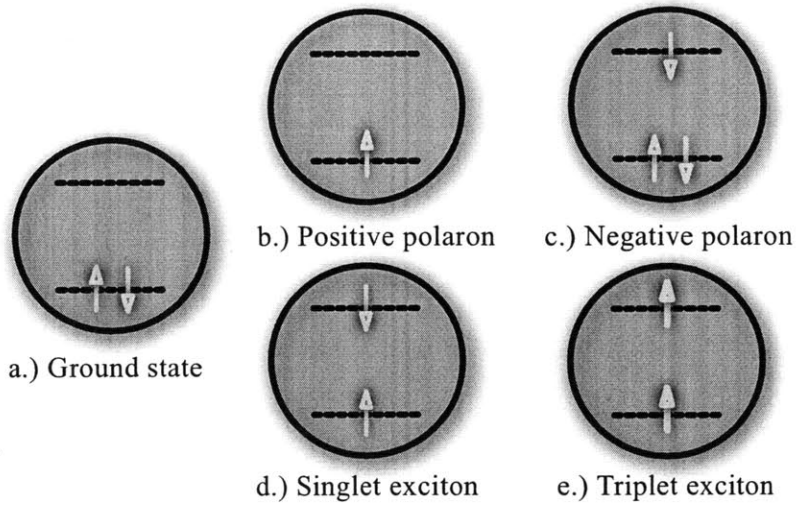

Figure 1-3: The basic excitations in an organic semiconductor. (a) A molecule in the ground state, seen as a fully occupied highest molecular orbital (HOMO). (b) A positive polaron, symbolized by a vacancy in the HOMO (c) A negative polaron, seen as an additional electron in the lowest unoccupied molecular orbital (LUMO) (d) A singlet exciton is a charge-neutral excitation with a total spin of one (e) A triplet exciton has zero total spin.

states for polarons and excitons are approximately Gaussian distributions with small variance (0.1-0.2 eV^2), [24] the occupation of states does not follow Fermi statistics [9, 17, 32]. Moreover, certain phenomena, such as carrier injection, may depend on spatial variations in the density of states due to the presence of defects, an electrostatic field, or other excitations [24].

1.2.2 Quantum dots

ONELab's use of colloidal quantum dots enable the group to easily integrate them into optoelectronic devices. Colloidal quantum dots are semiconductor nanocrystals with ligands attached to their surface so that they can be dissolved in a solution (Fig. 1-4). To make a device, the experimenter deposits a drop of QD solution on a spinning substrate. The drop spreads out and the solvent evaporates, leaving a uniform film of dots separated by ligands [3].

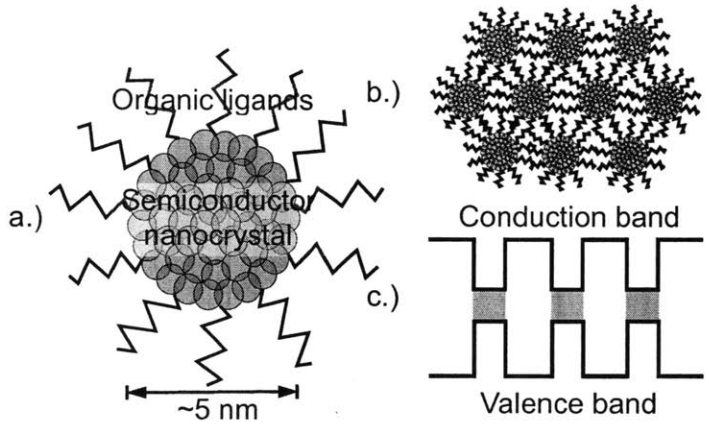

Figure 1-4: (a) A colloidal quantum dot is a semiconductor nanocrystal with organic ligands attached in order to make the dots soluble. (b) Quantum dot films are created by spin-coating: a drop of quantum dot solution is placed onto a spinning substrate. The solvent evaporates, leaving behind an ordered film, or superlattice, of quantum dots and ligands. (c) The band structure of the superlattice

Excitons, as in organic semiconductors, govern optical properties of quantum dots. In the simplest picture, a quantum dot is a real-life realization of a three-dimensional particle in a box (Fig. 1-4). By changing the width of the box, r, and the depth of the potential well, one can explain the r^{-2}-dependence of the quantum dot's exciton (band gap) energy [16]. Under the effective mass (parabolic band) approximation [6], quantum dots can be categorized by size: weak, strong, and intermediate confinement. Weak confinement occurs when the Bohr wavelength, r_B, is much larger than the crystal diameter. The Coulomb interaction, which is proportional to r^{-1}, dominates the r^{-2} nanocrystal size dependence. In the strong regime, nanocrystal size dominates the optical band gap. In the intermediate-regime, both effects must be taken into account [12].

For narrow band gap semiconductors and zincblende crystals, more complicated, six- or eight-band, Hamiltonians must be used to explain spectra because the parabolic band approximation fails. These effects may be important in optoelectronic applications, especially when long-lived "dark" exciton states reside within thermal activation energy of a singlet or triplet exciton states [2].

Chapter 2

Device physics

Modeling molecular electronic devices involves a trade-off between accuracy and complexity. Monte Carlo programs, such as those written by Bässler [9], Greenham [28], and Madigan [24], provide exact results at the cost of computation time. In order for a Monte Carlo simulation to model an amorphous material, each periodic unit cell must consist of thousands of molecules. In a full Monte Carlo simulation, each transfer rate at each time step must be computed. Simulating single layers, let alone entire devices, can take days on powerful machines [24].

Macroscopic models based on the continuity and drift-diffusion equations abstract away the complexity of the Monte Carlo approach in favor of computation speed [2, 49, 28]. Their output can provide phenomenological explanations of experimental results. However, the drift-diffusion equations may not be applicable to organic electronics (Sec. 1.2.1) because they assume operation near thermal equilibrium; the equations are derived from the first-order term in a perturbative solution to the Boltzmann equation [29]. Therefore, one must be cautious when interpreting these results. Moreover, the continuous nature of these differential equations complicates the process of adding the monomolecular or bimolecular processes inherent to organic semiconductors [1].

ONELab's thin film materials, whether organic semiconductors, colloidal quantum dots, or metal oxide films [53], share common characteristics: excitations are localized on specific molecules or (nano)crystals. While thermal hopping constitutes the ma-

jority of transport processes, long-range transport can also occur by Förster transfer or coherent quantum tunneling [2]. These commonalities suggest that the natural mathematical language to describe the operation of ONELab's devices is not that of continuous differential equations, but rather one of hopping, coupling, or tunneling between discrete, localized states.

The model proposed in this thesis attempts to find the middle ground between full Monte Carlo and drift-diffusion simulations. The overall thickness of ONELab's devices rarely exceeds hundreds of nanometers, while the length and width of the device are macroscopic quantities, typically on the order of one centimeter. Thus, to a charge localized on one molecule, the device appears to be nearly infinite in length and width. While excitations may find energetically-favorable percolation pathways on a local scale [35], the net flux of excitations along the length and width of the device averages to zero over increasingly larger areas.

A one-dimensional chain (Fig. 2-1) of discrete unit cells (this term will be used interchangeably with the words molecule or nanocrystal) should suffice to explain device behavior. Physically, each cell can be thought of as an ensemble average of all molecules or nanocrystals in the same plane. Reducing the dimensionality of the simulation is critical to making the code run quickly, since the number of nearest neighbors grows quickly with the number of dimensions. The quantities measured by ONELab experimentalists are macroscopic averages over an entire device area. Hence, the effects of disorder and nonequilibrium transport can be included in this one-dimensional framework by discretizing the density of states and keeping track of the relative occupation levels, as well as scattering events within each unit in the chain.

2.1 Mathematical description

In the one-dimensional chain model, the continuity equation and Gauss' Law govern all behavior. Steady-state operation occurs when the transfer rate into every cell equals the transfer rate out of that cell. At any given instant, the net transfer rate

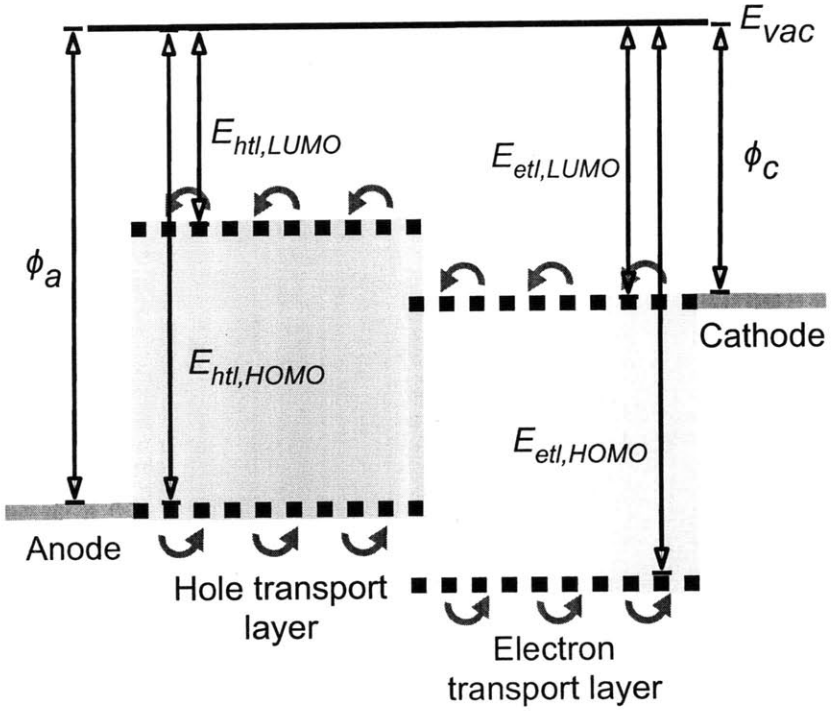

Figure 2-1: The two-layer device pictured above, with its corresponding band alignments, represents a typical ONELab device structure. The proposed model is a compromise between the band transport picture and a full Monte Carlo simulation. In this model, the HOMO/LUMO bands are discretized into unit cells, with each black dash representing one molecule. Bulk transport occurs by thermal hopping, symbolized by the red arrows. Additional processes (not shown above) can be easily added within this framework.

of a particular excitation, X, in the i^{th} unit cell is the difference between total rate into and the total rate out of that cell, according to the continuity equation.

$$\frac{dX_i}{dt} = \sum_{j \neq i} R_{j \to i} - R_{i \to j} \tag{2.1}$$

As charges move within the device, the relative energy levels of adjacent unit cells change in accordance with Gauss' Law.

$$\vec{\nabla} \vec{E} = \frac{4\pi e}{\epsilon_r}(p - n) \tag{2.2}$$

where p and n are the positive and negative polaron concentrations, respectively.

A particular excitation's transfer rate between two cells exhibits a dependence on both the relative occupation of the two cells and the potential difference between the cells. The transfer rate from an initial donor cell i to the final acceptor cell f is [34]

$$R_{i\to f} = \frac{1}{N_f}\int_{-\infty}^{\infty} dE_i \Gamma_i(E_i) f_i(E_i) \int_{-\infty}^{\infty} dE_f \Gamma_f(E_f)(1 - f_f(E_f))\nu(E_f - E_i) \qquad (2.3)$$

where $\Gamma_i(E_i)f(E_i)$ is the density of states *occupied* by X on the donor cell[1], $\Gamma_f(E_f)(1-f_f(E_f))$ is density of *unoccupied* sites on the acceptor cell, N_f is the total number of acceptor sites, and $\nu(E_f - E_i)$ is the energy-dependent hopping frequency, or rate, between the two sites. Physically, Eq. 2.3 represents a sum of the hopping rate over all possible energy differences between the two sites, weighted by the number of states available to participate in the process.

2.2 Relation with the drift-diffusion equation

Establishing a formal relation between the drift-diffusion equation and the one-dimensional hopping model allows estimations of hopping rates from experimentally-measurable quantities, such as carrier mobilities. This calculation will only be performed for polarons (denoted by p), but one could similarly derivate an expression for excitons. In classical semiconductor physics, the drift-diffusion equation for holes gives the hole current density, $\vec{J_p}$

$$\vec{J_p} = -D_p\vec{\nabla}p + e\mu_p p\vec{F} \qquad (2.4)$$

where $\vec{F}$ denotes the electric field. The hole flux is used in conjunction with the continuity equation to determine the time rate of change of the carrier concentration.

$$\frac{dp}{dt} = -\vec{\nabla}\cdot\vec{J_p} \qquad (2.5)$$

[1] Γ_i is the density of states function and f_i is the occupation probability

$\vec{F}$ is the electrostatic field and e is the fundamental charge, while μ_p and D_p are the material-specific carrier mobility and diffusivity, respectively. The mobility and diffusivity can be tensors if the material is anisotropic, but for the amorphous materials considered here, they are scalars [50]. For charged particles undergoing Brownian motion, the Einstein relation relates the mobility to the diffusivity [21, 13].

$$D_p = \frac{\mu_p k_b T}{e} \tag{2.6}$$

To relate the discrete hopping model to the drift-diffusion model, consider a system composed of three identical unit cells in a uniform field F_0 (Fig. 2-2). The hopping

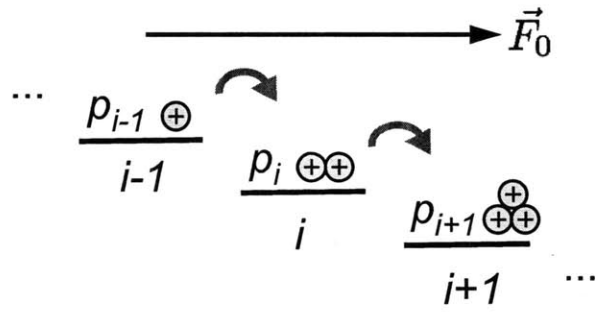

Figure 2-2: Polaron transport due to Miller-Abrahams thermal hopping. A uniform electric field, $\vec{F_0}$ is applied to three unit cells centered about cell i. Each cell's density of states is sharply peaked at the same energy, so the energy difference between sites is solely due to the electrostatic potential. The polaron concentrations are low enough such that the electric field does not change and there are many sites available for hopping.

frequencygiven by Miller-Abrahams theory [33] is a piecewise-continuous function based on the Arrhenius equation [22] and is frequently used to model excitation hopping in organic semiconductors [2, 7].

$$\nu_{MA}(E_f - E_i) = \begin{cases} K_0 \exp\left(-\frac{E_f - E_i}{k_b T}\right) & : E_f > E_i \\ K_0 & : E_f \leq E_i \end{cases} \tag{2.7}$$

The cells are separated by a uniform distance, d, so the energy difference between adjacent sites is $-eFd$.

In order to compute the hopping rates, one must make approximations in order to simplify the integral in Eq. 2.3. If each cell's density of states is a Dirac δ-function peaked at the same energy, $\Gamma(E_0) = N_i\delta(E - E_0)$, and the number of polarons on each site is much less than the number of available sites, $(N_f - p_f)/N_f \approx 1$, then the energy difference between sites is solely due to the electrostatic field. Therefore, the net transfer rate into cell i is simply

$$\frac{dp_i}{dt} = K_0\Big\{p_{i-1} - p_i - p_i \exp\left(\frac{-eF_0d}{k_bT}\right) + p_{i+1}\exp\left(\frac{-eF_0d}{k_bT}\right)\Big\} \tag{2.8}$$

Factoring out an exponential leads to the equivalent form

$$\frac{dp_i}{dt} = K_0 \exp\left(\frac{-eF_0d}{2k_bT}\right)\Big\{p_{i-1}\exp\left(\frac{eF_0d}{2k_bT}\right) - 2p_i\cosh\left(\frac{eF_0d}{2k_bT}\right) + p_{i+1}\exp\left(\frac{-eF_0d}{2k_bT}\right)\Big\} \tag{2.9}$$

Next, assume that the potential dropped across one molecule is less than the thermal energy, or $eF_0d << k_bT$. This is a reasonable approximation for most organic LEDs and solar cells, since they operate at low bias voltages: typical operating fields are on the order of 1×10^4 V/cm. This approximation breaks down when $F_0 \geq 2 \times 10^5$ V/cm. Expanding the exponentials and neglecting terms higher than first order leads to the result

$$\frac{dp_i}{dt} \approx K_0\Big\{(p_{i-1} - 2p_i + p_{i+1}) - \frac{ed}{2k_bT}F_0(p_{i+1} - p_{i-1})\Big\} \tag{2.10}$$

If the concentration, p, were a continuous function, then the terms in Eq. 2.10 would constitute centered finite difference approximations to the second and first derivatives of p, respectively [42]. In this limit, as $d \to 0$, Eq. 2.10 results in the following equation

$$\frac{dp_i}{dt} \approx -K_0d^2\Big\{-\nabla^2 p + \frac{e}{k_bT}F_0\nabla p\Big\} \tag{2.11}$$

By comparing Eq. 2.11 with Eqs. 2.4-2.5, a relation for K_0 can be established

$$K_0 = D_p/d^2 \tag{2.12}$$

$$K_0 = \mu_p k_b T/ed^2 \tag{2.13}$$

By equating Eqs. 2.12 and 2.13, one finds that the Einstein relation (Eq. 2.6) holds true for the one-dimensional hopping model in the limits of a narrow density of states, small field, and low carrier concentrations.

Chapter 3

Physical processes

Many physical processes occur simultaneously in organic semiconductors. Polarons of different polarity can interact with one another and with excitons while moving through the device. Excitons can also interact with photons, either being formed by photon absorption or decaying via photon emission. These processes are not always adiabatic; energy comes from coupling to a phonon bath [24]. Calculations of the spectrum of this phonon bath are nontrivial and computationally-intensive [24]. For the purposes of this thesis, where computation speed is a top priority, the Miller-Abrahams expression (Eq. 2.7) will describe the phonon bath.

3.1 Polarons

3.1.1 Thermal hopping

Polarons hop from molecule to molecule via phonon-mediated distortions of the local lattice (Fig. 3-1) [24]. The energy difference between two sites is equal to the change in local HOMO/LUMO levels plus the potential drop due to the electrostatic field. The rate constant in Miller-Abrahams theory, K_0, could be estimated from experimental measurements of the carrier mobility (Eq. 2.13 for polarons) or from the exciton diffusion length and lifetime (Eq. 2.12 for excitons) [2]. Alternatively, one could dynamically calculate K_0 from underlying theory.

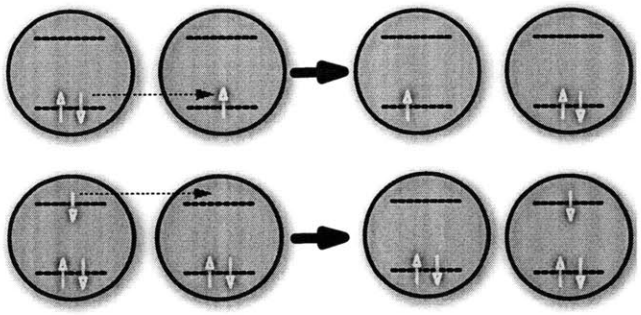

Figure 3-1: Polarons move by hopping between nearest neighbors. Since a polaron is not only a charged molecule, but also the surrounding lattice distortion, such a move is energetically unfavorable and requires energy from the phonon bath. The top diagram depicts positive polaron hopping, while the bottom picture shows hopping of a negative polaron.

Since adjacent molecules' (or nanocrystals') electronic wavefunctions have little overlap, outer shell Marcus theory appropriately describes the hopping transition rate between two unit cells [26, 7, 37]. Marcus theory follows from the Franck-Condon and Born-Oppenheimer approximations, where electrons move about a framework of static nuclei and the total wavefunction is the outer product of the nuclear, electron, and spin wavefunctions [16]. Since electrons move much faster than nuclei, the reaction coordinate is solely a function of nuclear positions between the initial and final states [10].

In its simplest version [26], Marcus theory assumes that the potential energy surfaces along the reaction pathway are parabolic about the initial and final states (Fig. 3-2). Marcus' insight was that energy must be conserved during electron transfer reactions. Energy conservation (and electron transfer) only occurs when the reactant nuclei undergo a thermal fluctuation along the reaction pathway, reaching the intersection of the two potential energy surfaces [26]. Marcus then applied Fermi's Golden Rule and computed the Franck-Condon overlap factors between the initial states, assuming that the nuclei could be approximated by displaced harmonic oscillators [16, 26]. In the high temperature limit, he was able to simplify the transfer

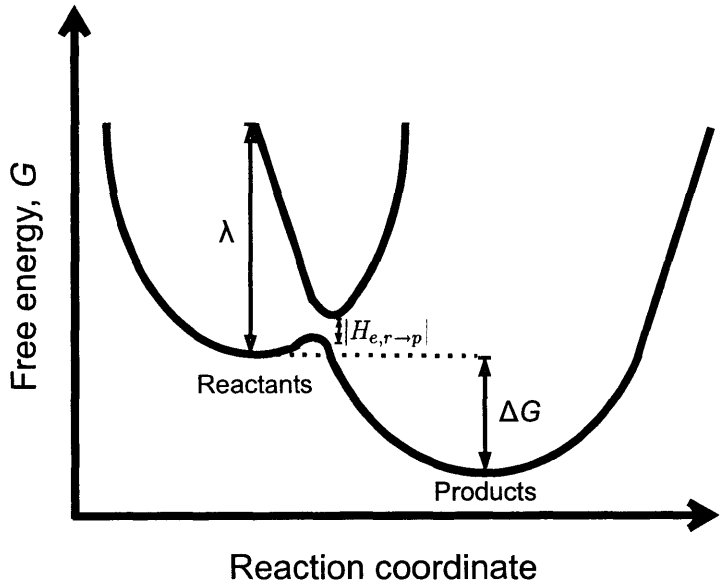

Figure 3-2: In Marcus theory, the reaction pathway is a function of the nuclear coordinates and the reaction surfaces are approximated by harmonic oscillators. The reorganization energy, λ, characterizes the overlap between the equilibrium product and reactant nuclear coordinates. The two potential energy surfaces split at their intersection due to weak electronic coupling. The electronic interaction Hamiltonian gives the prefactor for Marcus' rate expression, which shows a Gaussian dependence on the sum of the reorganization energy and free energy change, ΔG.

rate expression to

$$K_0 = \frac{2\pi}{\hbar} \frac{|H_{e,r\to p}|^2}{\sqrt{4\pi\lambda k_B T}} \exp\left(-\frac{(\lambda + \Delta G)^2}{4\lambda k_B T}\right) \tag{3.1}$$

where $H_{e,r\to p}$ is the matrix element of the perturbing electron interaction Hamiltonian [26]. Marcus theory's most surprising prediction is that of an inversion region, where the transfer rate decreases as the free energy change increases. This prediction, which wasn't confirmed until 1986, resulted in the award of a Nobel Prize in Chemistry to Marcus in 1992 [27].

Marcus theory is particularly important in organic electronics since important processes, such as exciton dissociation into free polarons [5], primarily occur at the interfaces between dissimilar materials. By changing energy level alignment, inter-

faces can be engineered to optimize rate processes via Eq. 3.1.

3.1.2 Polarization

The distribution of polaron states in organic semiconductors follows a Gaussian distribution [25]. Each molecules' static dipole moment interacts with the static dipole moments and charges on surrounding molecules. An applied electric field induces an additional polarization, which, from second order perturbation theory, is linear in the applied field [16]. Analytic and Monte Carlo studies agree; these homogeneous dipole-dipole interactions give rise to both a Gaussian density of states and a charge screening that is less than the $1/\epsilon$ screening in classical electromagnetism [25, 36].

Polarization effects can be easily incorporated into the framework of the one-dimensional hopping model. Since energy difference and distance between two sites determines the hopping rate [23], polarization contributes an additional term

$$\Delta E_{pol} = -(\vec{\mu}_2 \cdot \vec{F}_2 - \vec{\mu}_1 \cdot \vec{F}_1) + \frac{1}{2}(\alpha_2 |\vec{F}_2|^2 - \alpha_1 |\vec{F}_1|^2) \tag{3.2}$$

For a polaron, the change in polarization energy is much less than that due to the electrostatic potential. For an organic molecule, typical $\vec{\mu}$ and α values are on the order of 10 Debye and 1×10^{-20} cm^{-3} [36]. Typical operating fields for an LED or solar cell are $10^5 - 10^6$ V/cm [2] and concentrations on the order of 10^{16} cm^{-3}. Between two adjacent molecules, the difference in electrostatic potential is on the order of 50 meV, while the energy contributions from polarization are 1μeV and 0.1 neV[1] for the induced and static dipole moments, respectively. However, ΔE_{pol} could approach the electrostatic term's magnitude at high carrier concentrations ($>$ 10^{19} cm^{-3}). However, at these concentrations, dipole-dipole interactions may also become important. Unfortunately, such interactions are more difficult to include in the one-dimensional framework. Monte Carlo simulations must be employed at these concentrations [25].

[1]The static dipole moment was averaged over all possible orientations assuming a Boltzmann probability distribution as a function of the applied electrostatic field.

3.1.3 Recombination

Polarons of opposite polarity interact with one another in bimolecular processes, either annihilating one another or creating an exciton. In the former process, the energy from the recombination event can either cause photoemission of a third electron (Auger recombination), photon emission at a defect (radiative recombination), or multiphonon emission (non-radiative recombination) [41].

Exciton formation by means of Langevin recombination (Fig. 3-3) provides the

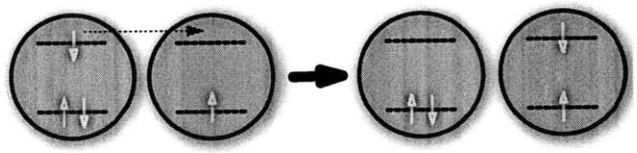

Figure 3-3: In Langevin recombination, two oppositely-charged polarons combine on the same molecule to form an exciton. The exciton can be either singlet or triplet, depending on the polaron spins and whether or not any phonon scattering occurs. Only the triplet case is shown above.

dominant mechanism for exciton creation and electroluminescence in OLEDs [2]. In Langevin recombination [41], the capture radius, R_c, is the distance at which the electrostatic energy of the polaron pair equals the average kinetic energy of each carrier, $e^2/\epsilon_r R_c = k_B T$. In a frame of reference where one polaron is stationary, the mobility is then $\mu_T = \mu_p + \mu_n$. Langevin then computed the drift current of one carrier in the electrostatic field of the other carrier, and found that the recombination rate is proportional to the product of the concentrations.

$$R_{\mathrm{L}} = \gamma_{np} np \tag{3.3}$$

where the rate constant, γ_{np}, is

$$\gamma_{np} = e\mu_T/\epsilon_r$$

3.1.4 Injection

In optoelectronic devices, carriers must move to and from a metal electrode into the device's active layers. The electrodes function like reservoirs of charge, but the exact nature of the hopping process from delocalized states in the metal to localized states in the semiconductor is still a matter of debate [4, 7, 46]. Experimental results based on ultraviolet photoemission spectroscopy and inverse photoelectron spectroscopy [39, 47] agree with *ab initio* [20, 52] calculations based upon Density Functional Theory. The adsorption of organic molecules on a metal surface can slightly change the Fermi level of the metal and, more importantly, can result in the formation of a surface dipole, as charge is transferred from the metal to the organic. Additionally, chemical reactions between the metal and organic can result in the formation of trap states that lie within the HOMO-LUMO energy gap [39, 47].

Several different models for carrier injection rates as functions of the applied field exist. In the simple, unrealistic picture of Ohmic injection [49], the injected current is the drift current at the electrode, $\vec{J}_{inj} = e\mu p\vec{F}$. Scott and Malliaras' injection model, which is based on thermionic injection over a potential barrier, has gained popularity on the modeling community [46]. A third model, proposed by Baldo et al. [7, 23], rests on a microscopic picture of interface dynamics. The rate-limiting step is not the initial hop from the metal to the organic, but the hop from the first organic layer to the second. This model reproduces the correct power law in experimental current-voltage curves over a narrow range of bias voltages and temperatures [23].

3.2 Excitons

The study of exciton motion in organic semiconductors plays a crucial role in the development of optoelectronic devices. Photons can be converted to and from free charge carriers via the formation or radiative decay of an exciton. In OLEDs, the location of exciton decay determines the color of photon emission [2]. In solar cells, on the other hand, high efficiencies can only be obtained when excitons are transported before they decay to an interface, where they dissociate into the free polaron pairs

that can be harvested for current [40]. Excitons can be converted from singlet to triplet and vice versa by spin-orbit coupling [8] or phonon scattering [41]. Each of these processes occurs at a characteristic rate in different materials.

3.2.1 Förster transfer of singlet excitons

Singlet excitons can travel from molecule to molecule by dipole-to-dipole coupling (Fig. 3-4) [41]. The rate decays as the sixth power of the intermolecular distance,

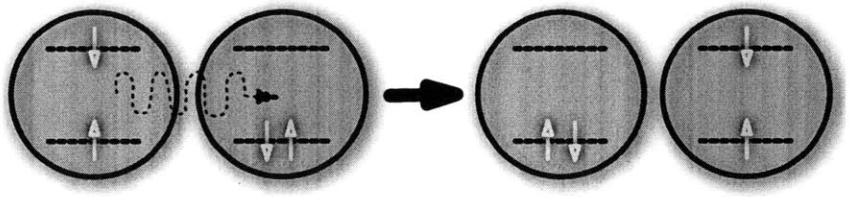

Figure 3-4: In Förster transfer, a singlet exciton couples its dipole moment to a molecule in the ground state, resulting in the transfer of the excitation. This dipole coupling is shown above by the (virtual) photon, even though no photons are exchanged in Förster transfer.

since the donor's dipole field decays as R^{-3} and the induced dipole on the acceptor is proportional to R^{-3} [18]. The overlap of the normalized donor emission spectrum, $F_D(\omega)$, and acceptor absorption spectrum, $\sigma_A(\omega)$, gives the transition rate constant [15].

$$\nu_{D\to A} = \frac{3c^4}{4\pi\epsilon_D^4}\frac{1}{\tau_D}\frac{1}{R^6}\int \frac{1}{\omega^4}F_D(\omega)\sigma_A(\omega)d\omega \tag{3.4}$$

3.2.2 Dexter transfer

Although triplet excitons cannot undergo Förster transfer because of quantum mechanical selection rules [16], they can couple to other molecules via higher multipole interactions or by electron exchange. The latter case is the dominant rate for triplet-triplet energy transfer, in which two electrons simultaneously switch places (Fig. 3-5) [41]. Since this electron exchange hopping process requires wavefunction overlap, Dexter transfer is a nearest-neighbor hopping mechanism. The hopping rate expression, calculated from Fermi's Golden Rule, depends on the overlap between the donor

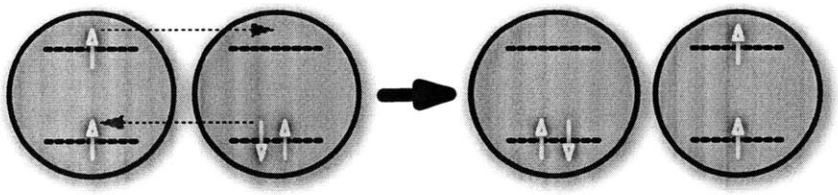

Figure 3-5: Dexter transfer is the movement of an exciton, either singlet or triplet, by the simultaneous exchange of two electrons.

phosphorescence and acceptor absorption spectra [11]. Since these spectra are not readily available, this work uses experimentally-measured exciton diffusion lengths and lifetimes to estimate Dexter transfer rates.

3.2.3 Photons

Excitons can be formed by absorption of a photon and photons can be emitted by the radiative decay of a singlet exciton. The net rate of exciton formation from an external electromagnetic field is the difference between the absorption rate and radiative recombination rate

$$\nu_G = -\frac{1}{\tau} + \int_0^\infty G(\omega) d\omega \tag{3.5}$$

where τ is the exciton lifetime and $G(\omega)$ is the generation function, which is dependent on the frequency of the applied electromagnetic field (Fig. 3-6). $G(\omega)$ is the net photon generation rate, taking both absorption and stimulated emission into account. It can be determined from applying the Franck-Condon principle and Fermi's Golden Rule to a molecule with a known absorption spectrum [10, 16, 24].

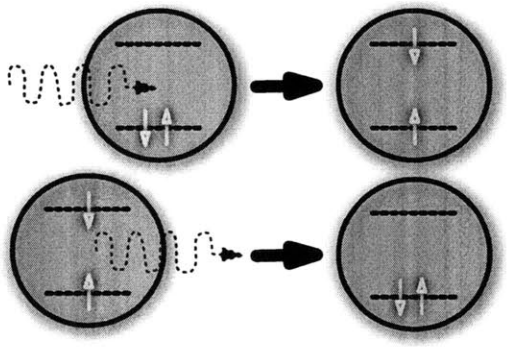

Figure 3-6: Photon absorption and emission result in the creation or decay of a singlet exciton, respectively.

Chapter 4

Numerical simulation

The one-dimensional hopping model in Section 2 is not amenable to an analytic solution [9]. For realistic device structures with many competing rate processes, it must be solved numerically. Implementing such a numerical model requires projecting the device physics onto a convenient language for computation.

4.1 Programming language

The numerical simulation was written in the Python programming language. Python was selected because it is a high-level, open-source programming language with automatic memory management [43]. Python is portable between different operating systems and supports multiple programming paradigms, from functional to object-oriented programming. Moreover, the linear algebra library, NumPy, in conjunction with the scientific library, SciPy, and the plotting libarary, MatPlotLib, lends Python nearly all of the capabilities of the widely-used, proprietary MATLAB software suite. Although Python is not as fast as C++ or FORTRAN [43], its large user base, selection of libraries, and usability will encourage future collaboration, modifications, and additions to the code.

4.2 Methodology

The object-oriented programming paradigm forms the basis for the one-dimensional hopping model simulation code. This programming technique suits the nature of the problem; a device is a collection of discrete molecules or nanocrystals and the rate processes between them. Fig. 4-1 diagrams the basic objects and their interaction in

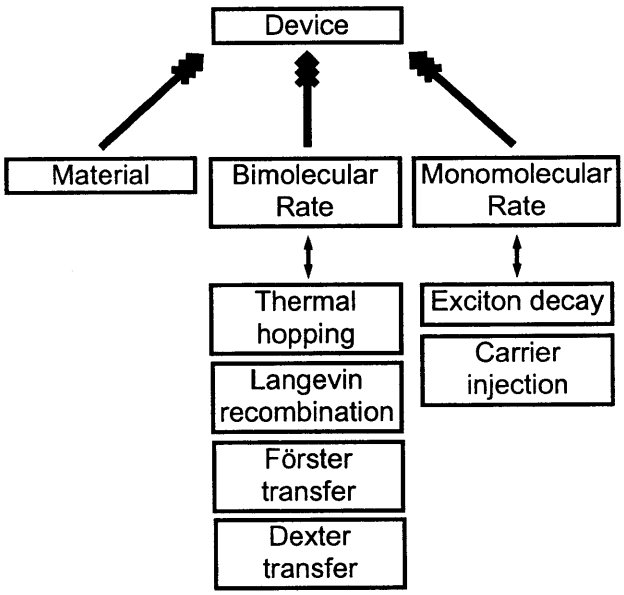

Figure 4-1: The class hierarchy used in order to model the one-dimensional chain. Double-sided arrows indicate a parent-child class relationship, while the barbed arrows indicate that a class is a data structure within another class. Decoupling the physical description of a device (number of molecules and material type) from the rate processes connecting the individual molecules makes the model adaptable.

this simulation.

A collection of `Material` and `Rate` objects constitute a `Device`. The `Material` keeps track of the experimentally-measurable properties of a certain material, such as polaron mobilities and exciton lifetimes. `Rate` objects are subdivided into two types, `Bimolecular Rates` and `Monomolecular Rates` in order to specify if a rate process takes place within one layer (e.g. radiative exciton decay) or between layers (e.g. nearest-neighbor hopping, Förster transfer).

To conduct a simulation, the user sends a list of operating voltages to the `Device` class. Then, for each voltage, the `Device` integrates the polaron and exciton concentrations in discrete time steps using a 4th order Runge-Kutta method. At each infinitesimal displacement in time, the simulation adjusts the electric field such that the total voltage drop over the entire device is constant. This is equivalent to a real-world experiment where a device is connected to a voltage source. The run terminates when the integration time limit is exceeded or the displacement current (due to the time rate of change of the electric field) drops below a user-defined threshold. At user-specified time intervals, the solver records the current density, polaron and exciton concentrations, and the electrostatic field and potential.

4.3 Results

The validity of the one-dimensional hopping model can be established by completing increasingly complicated simulations and comparing results with experiment. For these initial simulations, simplifications were made in order to speed computation time and to avoid increasing the model's complexity before the core modeling concept, the one-dimensional chain, could be verified. For the simulations presented in this work, all `Materials'` densities of states were delta functions. Moreover, the thermal polaron hopping rate was constant instead of dynamically-calculated using Marcus theory (Eq. 3.1). Excitons were formed in the bulk or at internal interfaces by Langevin recombination. Finally, Förster transfer of excitons was not included, so exciton motion was purely diffusive by Dexter transfer.

4.3.1 Simple numerical experiment

A simple, symmetric diode structure was selected for the initial experiment (Fig. 4-2). The parameters were chosen such that the polaron concentrations should show a reflection symmetry, e.g. the positive polaron concentration is a reflection of the negative polaron concentration about the center of the device. Tables 4.1 and 4.2 summarize the material parameters used for these simulations.

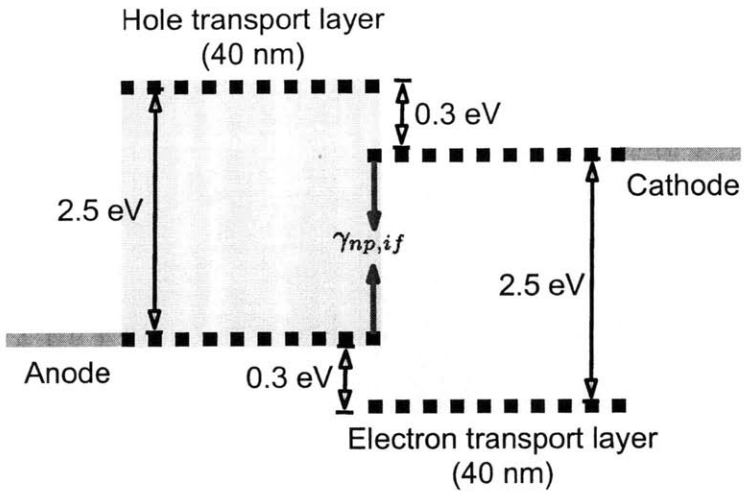

Figure 4-2: Symmetric two-layer device structure chosen for the initial computational experiment. The hole mobility of the hole transport layer was 1×10^{-3} cm^2/V-s and the electron mobility was 1×10^{-6} cm^2/V-s. The electron transport layer's mobilities were the opposite. While keeping other device parameters constant, the bimolecular interfacial recombination rate $\gamma_{np,if}$ was varied.

Layer	Thickness [cm]	μ_p [cm^2/V-s]	μ_n [cm^2/V-s]	E_L [eV]	E_H [eV]	$\gamma_{np,bulk}$ [cm^3/s]
Hole transport	4×10^{-6}	1×10^{-3}	1×10^{-6}	2.1	5.1	1×10^{-14}
Electron transport	4×10^{-6}	1×10^{-6}	1×10^{-3}	2.4	5.4	1×10^{-14}

Table 4.1: Polaron transport parameters for simulating the symmetric device structure. The Miller-Abrahams hopping rates were calculated from the mobilities (μ) and the energy level difference at the interface (E_H and E_L). Langevin recombination in the bulk formed excitons from polaron recombination, with a rate constant $\gamma_{np,bulk}$.

In this experiment, the bimolecular interfacial recombination rate, $\gamma_{np,if}$ (Eq. 3.3), was varied over eight orders of magnitude, from 1×10^{-8} to 1×10^{-16} cm^3/s. Malliaras and Scott's injection model was used [46] with no injection barriers. Each device structure was simulated at biases ranging from 0.5 to 10 V and the transient results were recorded at intervals of 1 μs.

Fig. 4-3 shows the positive polaron concentration profiles as a function of the interfacial recombination rate. The drift-diffusion equations can be used to explain the results qualitatively. The positive and negative polaron (not pictured) concentrations

Layer	Thickness [cm]	E_g [eV]	L_x [cm	τ_x [s]
Hole transport	4×10^{-6}	2.5	1×10^{-6}	1×10^{-7}
Electron transport	4×10^{-6}	2.5	1×10^{-3}	1×10^{-7}

Table 4.2: Exciton transport parameters for simulating the symmetric device structure. The Miller-Abrahams hopping rates were calculated from the exciton diffusion length, L_x, and lifetime, τ_x.

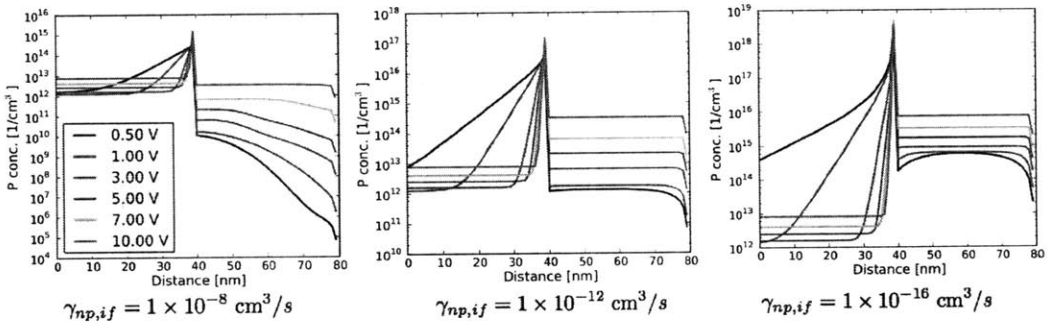

Figure 4-3: Positive polaron concentrations as a function of distance from the anode. As expected, the negative polaron concentrations were an exact reflection of the positive polaron concentrations about the center of the device. As the interfacial recombination rate decreased, more charge built up at the interface in order to ensure current continuity.

were mirror images of one another, confirming the expected hypothetical solution. At low bias voltages, the concentration gradient in the hole transport layer was positive, creating a diffusion current to oppose the drift current. At higher biases, drift dominated. The exciton concentration profile (not shown) was nearly flat across the device, since the band gap of each material was the same and exciton diffusion was relatively fast (ns) as compared to exciton formation (μs).

The field profile (Fig. 4-4) was consistent with the trends in concentration profiles. The electric field equal at both electrodes, indicating that there is no space charge buildup within the device. The lack of space charge is a direct consequence of the symmetry of the polaron concentration profiles. At low recombination rates and bias voltages, the weak electric field could not push carriers over the thermal barrier, resulting in charge accumulation and a field spike. The carrier and field spikes ensured current continuity two different ways. First, the sharp gradient introduced a diffusion

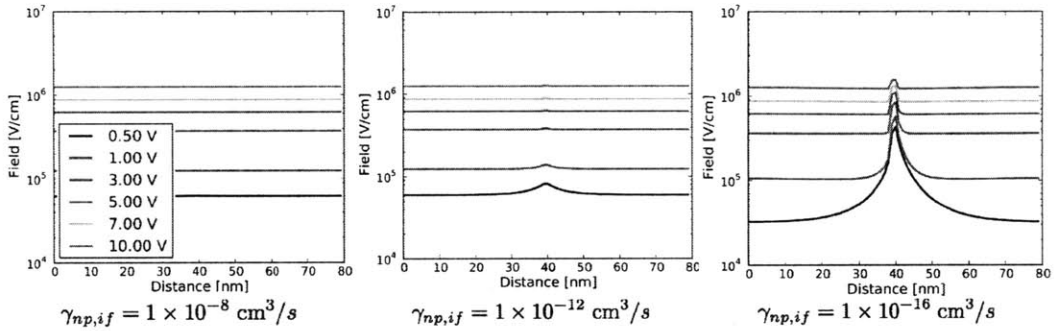

Figure 4-4: Electrostatic field as a function of distance from the anode. At low recombination rates and voltages, the electric field spiked at the device center due to carrier accumulation on each side of the heterojunction.

current away from the interface to compensate for the drift. Simultaneously, the field spike slightly lowered the effective thermal barrier at the interface, increasing the current across the barrier until it equaled the net current arriving at the interface. The devices with lower interfacial recombination rates required longer integration times to reach steady state operation because of the time taken to form the interfacial field spike.

4.3.2 Comparison with experiment

In order to compare the hopping models' results with experiment, a "real" OLED structure was modeled. The first OLED fabricated by Tang et. al. in 1987 was a bilayer device composed of the hole-transporting material TPD[1] and the electron-transporting material Alq_3[2] [51]. The simplifications of a delta-function density of states, constant hopping rates, and nearest-neighbor exciton transport were used again and both the hole and electron transport layers were taken to be 40 nm thick. As before, the polaron and exciton hopping rates were calculated from experimental mobilities using Eqs. 2.12-2.13, enabling direct comparison with past drift-diffusion simulations (Tables 4.3-4.4) [2].

The injection model had the largest impact on the solution since it dictated the

[1] N,N'-bis(3-methylphenyl)-N,N'-44 bis(phenyl)benzidine
[2] tris-(8-hydroxyquinoline) aluminum

Layer	Thickness [cm]	μ_p [cm^2/V-s]	μ_n [cm^2/V-s]	E_L [eV]	E_H [eV]	$\gamma_{np,bulk}$ [cm^3/s]
TPD	4×10^{-6}	1.25×10^{-3}	1.88×10^{-7}	2.1	5.4	1×10^{-14}
Alq_3	4×10^{-6}	1×10^{-7}	1×10^{-5}	3.1	5.8	1×10^{-14}

Table 4.3: Polaron transport parameters for simulating the TPD-Alq_3 bilayer OLED. The Miller-Abrahams hopping rates were calculated from the mobilities (μ) and the energy level difference at the interface (E_H and E_L). Langevin recombination in the bulk formed excitons from polaron recombination, with a rate constant $\gamma_{np,bulk}$.

Layer	Thickness [cm]	E_g [eV]	L_x [cm	τ_x [s]
TPD	4×10^{-6}	2.6	1×10^{-7}	1×10^{-7}
Alq_3	4×10^{-6}	2.4	8×10^{-7}	1×10^{-8}

Table 4.4: Exciton transport parameters for simulating the TPD-Alq_3 bilayer OLED. The Miller-Abrahams hopping rates were calculated from the exciton diffusion length, L_x, and lifetime, τ_x.

boundary conditions. The author implemented several injection models, including Ohmic contacts, constant carrier concentrations [2], Scott and Malliaras' thermionic injection model [46], Baldo and Forrest's microscopic model [7], and Limketkai and Baldo's microscopic model [23]. The last model, with its derivation of a simple power law for the injected current, achieved the best agreement with experiment and is presented below. Identical parameters were chosen for the anode and cathode: the injected current was proportional to the 20^{th} power of the applied field.

The difference in material parameters broke the symmetry of the previous device's solutions. Fig. 4-5 shows the polaron and exciton concentration profiles after convergence. The majority of the excitons diffused into the lower-bandgap Alq_3 material, as expected from experimental observations of device emission [2].

The polaron profiles indicate two regimes of operation which can be phenomenologically explained by the drift-diffusion equations. At biases less than 3 V, the polaron profiles resemble those from the previous simulation; the concentrations near the electrode and internal interface are relatively independent of the applied field. Increasing the field, in analogy to the classic PN junction [6], narrows the organic-semiconductor-equivalent of a "depletion region" [3] because the increase in drift cur-

[3] In inorganic semiconductor homojunctions, the depletion region is composed of charge carri-

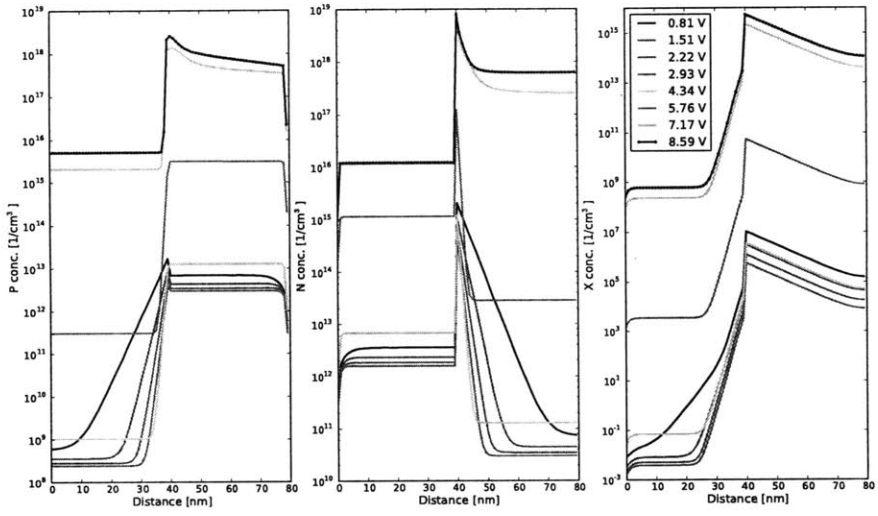

Figure 4-5: Polaron and exciton concentration as a function of distance from the anode. . Nearly all excitons (right), diffused into the lower band gap Alq_3 material, in accordance with the observed device emission [51].

rent balances a sharper concentration gradient at the interface. At higher biases, the larger electrostatic field begins to push positive polarons over the 0.3 eV HOMO offset. Negative polarons, however, remain stuck on the Alq_3 side of the interface due to the larger (0.6 eV) LUMO offset. Transport of negative polarons becomes negligible and they accumulate at the TPD-Alq_3 interface, bending the energy levels of Alq_3 (Fig. 4-6).

Since experimentalists have not measured the charge or field cross-sections of their thin devices [2, 3, 24], there is no way to compare the polaron concentration profiles with experiment. However, one can easily compare numerical simulations' current-voltage (J-V) characteristics with experiment (Fig. 4-7).

The one-dimensional model described in this thesis reproduced experimental current-voltage characteristics over a wide range of bias voltages. Previous simulations with a drift-diffusion model [1], could not reproduce low-bias J-V curve due to neglect

ers opposite to the polarity of the dopant. In organic heterojunctions, the HOMO-LUMO energy difference prevents minority carriers from diffusing across the interface.

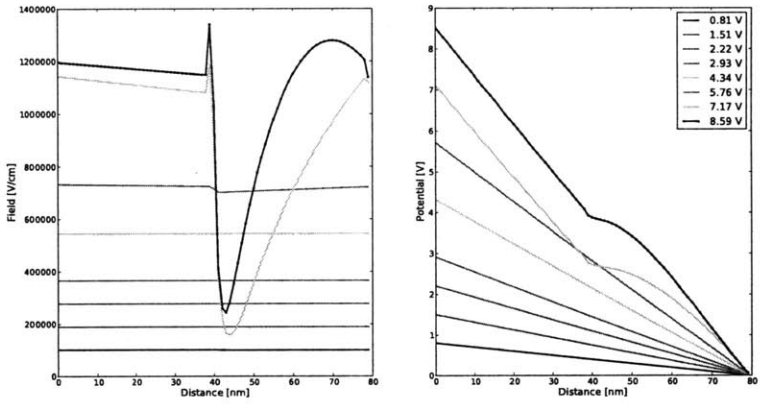

Figure 4-6: The electrostatic field (left) was constant across the device at low bias voltages, in accordance with the picture that energy level (band) diagrams in organic semiconductors have little curvature due to space charge [3]. At high biases, however, charge accumulation at the interface results in slight bending (right).

of diffusion currents at the electrodes. The hopping model effectively captured this behavior and Lamtekai's injection model accounted for the power law relationship at turn-on. Above 7 V, the hopping model reproduced the change in slope of the experimental J-V curve; the kink indicates that the rate-limiting process within the device changed; the rate of hole-hopping from TPD to Alq_3, rather than the injected current, became the limiting process. Perhaps, by changing the injection model parameters and HOMO energy offset at the TPD-Alq_3 interface, this model could achieve better agreement with experiment.

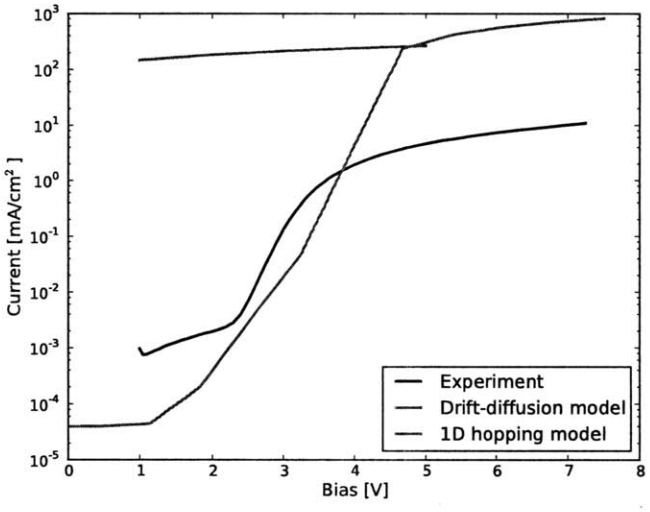

Figure 4-7: A comparison of experimental and numerical results for the current-voltage characteristics of the TPD-Alq_3 OLED. The hopping model presented in this work achieved better agreement with experiment due to inclusion of the recombination current at the electrode-organic interface, which was neglected in the drift-diffusion model.

Chapter 5

Conclusions

This thesis' one-dimensional chain model attempted to combine the most desirable features of drift-diffusion and Monte Carlo device simulation techniques. In certain limits, the chain model reduced to the drift-diffusion equations and preserved Einstein's relation. The chain model could be thought of an approximation to a spatially-averaged Monte Carlo simulation; it could account for nonequilibrium transport between localized states. Moreover, the computational framework surrounding the implementation could be easily modified; any rate process involving excitons or polarons could be incorporated into the model in less than twenty lines of code.

In order to test the one-dimensional chain model, two numerical experiments were performed. In the first, a simple test case, a symmetric device structure was chosen and a symmetric solution ansatz proposed. The calculation confirmed this hypothesis and then the effect of bimolecular interfacial recombination was explored. The numerical results showed that decreasing the interfacial recombination rate lead to increased charge accumulation at the interface, resulting in the formation of a spike in the electrostatic field. Finally, a real-world TPD-Alq_3 OLED was modeled and results were compared with experiment. The organic semiconductor-equivalent of a depletion region was formed and its thickness varied in analogous manner to that of an inorganic PN junction [6]. The excitons also diffused into Alq_3, as expected from experiment. Furthermore, the numerical results matched the experimental current-voltage characteristics over a wide range of bias voltages. To the best of the author's

knowledge, this is the first time that this has been accomplished without resorting to Monte Carlo techniques.

5.1 Further work

The one-dimensional chain model and associated computational framework yielded promising results. These results should be compared with Monte Carlo simulations. At high biases, the high fields and carrier concentrations could result in a breakdown of the assumptions implicit in this work, such as neglect of dipole-dipole interactions and the delta-function density of states. Additionally, further refinement will move the simulation code closer order to the goals outlined at the beginning of this thesis: agreement with experiment, computational speed, and usability.

5.1.1 Refinements to the physical model

Experimental work must go hand-in-hand with simulation; starting with the simplest, single-layer and single-carrier devices, parameters should be extracted to plug into the numerical model. Incrementally increasing the device and simulation complexity at each step will allow ONELab members to establish controls and isolate the effects of different processes from one another. Although the model in this thesis was relatively simple, the model's complexity could eventually increase in order to predict real-world device performance. Some of the features to be implemented are described below.

- **Generalized density of states**

  Only Dirac δ-function densities of state were considered in thesis in order to simplify the simulation. To model nonequilibrium transport, the simulation must account for any arbitrary density of states function. Using spectral decompositions of both the density of states functions, Γ_i, and the occupation functions, f_i, would allow the integrals to be quickly computed while maintaining the fast convergence properties associated with spectral methods [42].

- **Long-range transport**

Both Förster resonant energy transfer of singlet excitons and long-range transport by quantum tunneling were not included in the simulations in this paper. These effects can be important in devices incorporating quantum dot films and charge blocking layers [2].

- **Ionization in quantum dots**

  In some of ONELab's LEDs with quantum dots [54], electroluminescence occurs even if one carrier is injected into the device. The proposed mechanism for creation of the opposite carrier involves quantum tunneling across the band gap at high electrostatic fields. The field-dependence of this rate will have to be derived, either using the WKB approximation or Fermi's Golden Rule [16], before being inserted into the model.

Bibliography

[1] P. O. Anikeeva, I. M. Rousseau, and V. Bulović. Unpublished manuscript, 2009.

[2] P.O. Anikeeva. *Physical properties and design of light-emitting devices based on organic materials and nanoparticles.* MIT Dept. of Electrical Engineering and Computer Science. PhD Thesis, 2009.

[3] A.C. Arango. *A quantum dot heterojunction photodetector.* MIT Dept. of Electrical Engineering and Computer Science. SM Thesis, 2005.

[4] V. I. Arkhipov, E. V. Emelianova, Y. H. Tak, and H. Bassler. Charge injection into light-emitting diodes: Theory and experiment. *Journal of Applied Physics*, 84(2):848–856, July 15, 1998 1998.

[5] V. I. Arkhipov, P. Heremans, and H. Bassler. Why is exciton dissociation so efficient at the interface between a conjugated polymer and an electron acceptor? *Applied Physics Letters*, 82(25):4605–4607, 2003.

[6] N. W. Ashcroft and N. D. Mermin. *Solid state physics.* Saunders College Pub., Fort Worth, 1976.

[7] M. A. Baldo and S. R. Forrest. Interface-limited injection in amorphous organic semiconductors. *Physical Review B*, 64(8):085201, 08/07 2001.

[8] M. A. Baldo, D. F. O'Brien, Y. You, A. Shoustikov, S. Sibley, M. E. Thompson, and S. R. Forrest. Highly efficient phosphorescent emission from organic electroluminescent devices. *Nature*, 395(6698):151–154, 09/10 1998. M3: 10.1038/25954; 10.1038/25954.

[9] H. Bässler. Charge transport in disordered organic photoconductors a monte carlo simulation study. *Physica Status Solidi B*, 175(1):15–56, 1993.

[10] E. U. Condon. The franck-condon principle and related topics. *American Journal of Physics*, 15(5):365–374, September 1947 1947.

[11] D. L. Dexter. A theory of sensitized luminescence in solids. *The Journal of Chemical Physics*, 21(5):836–850, 1953.

[12] A.L. Efros and M. Rosen. The electronic structure of semiconductor nanocrystals. *Annual Review of Materials Science*, 30(1):475–521, 08/01 2000.

[13] A. Einstein. ber die von der molekularkinetischen theorie der wrme geforderte bewegung von in ruhenden flssigkeiten suspendierten teilchen. *Annalen der Physik*, 322(8):549–560, 1905.

[14] S. R. Forrest. The path to ubiquitous and low-cost organic electronic appliances on plastic. *Nature*, 428(6986):911–918, 04/29 2004.

[15] T. Förster. Zwischenmolekulare energiewanderung und fluoreszenz. *Annalen der Physik*, 437(1-2):55–75, 1948.

[16] D. J. Griffiths. *Introduction to quantum mechanics.* Pearson Prentice Hall, Upper Saddle River, NJ, 2 edition, 2005.

[17] K. Huang. *Introduction to statistical physics.* CRC Press, Boca Raton, 2 edition, 2009.

[18] V. M. Kenkre and R. S. Knox. Theory of fast and slow excitation transfer rates. *Physical Review Letters*, 33(14):803, 09/30 1974.

[19] V. I. Klimov. *Semiconductor and metal nanocrystals : synthesis and electronic and optical properties.* Marcel Dekker, New York, 2004.

[20] N. Koch, G. Heimel, J. Wu, E. Zojer, R. L. Johnson, J. L. Brdas, K. Mllen, and J. P. Rabe. Influence of molecular conformation on organic/metal interface energetics. *Chemical Physics Letters*, 413(4-6):390–395, 9/26 2005.

[21] R. Kubo. The fluctuation-dissipation theorem. *Reports on Progress in Physics*, (1):255, 1966.

[22] Keith J. Laidler. *Chemical kinetics.* HarperCollins, New York, 3 edition, 1987.

[23] B.N. Limketkai. *Charge Carrier Transport in Amorphous Organic Semiconductors.* MIT Dept. of Electrical Engineering and Computer Science. PhD Thesis, 2008.

[24] C. Madigan. *Theory and simulation of amorphous organic electronic devices.* Massachusetts Institute of Technology. Dept. of Electrical Engineering and Computer Science, 2006.

[25] C. M. Madigan and V. Bulović. Charge carrier energy disorder in polar amorphous organic thin films. *Applied Physics Letters*, 97(21):216402, 2006.

[26] R. A. Marcus. Chemical and electrochemical electron-transfer theory. *Annual Review of Physical Chemistry*, 15(1):155–196, 10/01 1964.

[27] R. A. Marcus. Nobel prize lecture in chemistry, 1992.

[28] R. A. Marsh, C. Groves, and N. C. Greenham. A microscopic model for the behavior of nanostructured organic photovoltaic devices. *Journal of Applied Physics*, 101(8):083509, 2007.

[29] A. H. Marshak and C. M. Van Vliet. Electrical current and carrier density in degenerate materials with nonuniform band structure. *Proceedings of the IEEE*, 72(2):148–164, 1984.

[30] S. A. McDonald, G. Konstantatos, S. Zhang, P. W. Cyr, E. J. D. Klem, L. Levina, and E. H. Sargent. Solution-processed pbs quantum dot infrared photodetectors and photovoltaics. *Nature Materials*, 4(2):138–142, print 2005.

[31] J. McGinness, P. Corry, and P. Proctor. Amorphous semiconductor switching in melanins. *Science*, 183(4127):853–855, March 1 1974.

[32] James A. McLennan. *Introduction to nonequilibrium statistical mechanics.* Prentice Hall advanced reference series. Prentice Hall, Englewood Cliffs, N.J., 1989.

[33] A. Miller and E. Abrahams. Impurity conduction at low concentrations. *Physical Review*, 120(3):745, 11/01 1960.

[34] B. Movaghar. Diffusion and relaxation of energy in disordered organic and inorganic materials. *Physical Review B*, 33(8):5545, 1986.

[35] B. Movaghar and W. Schirmacher. On the theory of hopping conductivity in disordered systems. *Journal of Physics C: Solid State Physics*, (6):859, 1981.

[36] Yuki Nagata. Polarizable atomistic calculation of site energy disorder in amorphous alq3. *Chem. Phys. Chem.*, 11(2):474–479, 2010.

[37] J. Nelson, J. Kirkpatrick, and P. Ravirajan. Factors limiting the efficiency of molecular photovoltaic devices. *Physical Review B*, 69(3):035337, Jan 2004.

[38] OSRAM Opto SemiconductorGmbH. Oled lighting project, 2008.

[39] H. Peisert, M. Knupfer, and J. Fink. Energy level alignment at organic/metal interfaces: Dipole and ionization potential. *Applied Physics Letters*, 81(13):2400–2402, September 23, 2002 2002.

[40] P. Peumans, A. Yakimov, and S. R. Forrest. Small molecular weight organic thin-film photodetectors and solar cells. *Journal of Applied Physics*, 93(7):3693–3723, April 1, 2003 2003.

[41] M. Pope and C. E. Swenberg. *Electronic processes in organic crystals.* Oxford science publications. Clarendon Press; Oxford University Press, Oxford; New York, 1982.

[42] William H. Press. *Numerical recipes : the art of scientific computing.* Cambridge University Press, Cambridge, UK ; New York, 3 edition, 2007.

[43] Python Software Foundation. Python documentation, 2010.

[44] QD Vision. Company website, 2010.

[45] Royal Philips Electronics. Oled lighting project, 2009.

[46] J. C. Scott and G. G. Malliaras. Charge injection and recombination at the metalorganic interface. *Chemical Physics Letters*, 299(2):115–119, 1/6 1999.

[47] K. Seki, N. Hayashi, H. Oji, E. Ito, Y. Ouchi, and H. Ishii. Electronic structure of organic/metal interfaces. *Thin Solid Films*, 393(1-2):298–303, 8/1 2001.

[48] Sony Corporation. Xel-1 oled television, 2008.

[49] J. Staudigel, M. Stossel, F. Steuber, and J. Simmerer. A quantitative numerical model of multilayer vapor-deposited organic light emitting diodes. *Journal of Applied Physics*, 86(7):3895–3910, October 1, 1999 1999.

[50] S. M. Sze and Kwok K. Ng. *Physics of semiconductor devices.* Wiley-Interscience, Hoboken, N.J., 3 edition, 2007.

[51] C. W. Tang and S. A. VanSlyke. Organic electroluminescent diodes. *Applied Physics Letters*, 51(12):913–915, September 21, 1987 1987.

[52] G. Witte, S. Lukas, P. S. Bagus, and C. Woll. Vacuum level alignment at organic/metal junctions: "cushion" effect and the interface dipole. *Applied Physics Letters*, 87(26):263502, 26 December 2005 2005.

[53] V. C. Wood. *All inorganic colloidal quantum dot LEDs.* MIT Dept. of Electrical Engineering and Computer Science. SM Thesis, 2007.

[54] V. C. Wood, M. Panzer, and V. Bulović. Unpublished manuscript, 2010.

[55] J. Xue, B. P. Rand, and S. R. Forrest. Origin of the open-circuit voltage in organic solar cells. 6334:63340K, August 31, 2006 2006.